photonics

MDPI

Article

Propagation Properties of Non-Diffracting Tricomi Beam in Atmospheric Turbulence

Lin Ma [1,*], Haibo Niu [1,2], Xingxing Han [1], Youzhang Zhu [1,2] and Jing Shi [1,2]

[1] School of Intelligent Manufacturing and New Energy, Xi'an Jiaotong University City College, Xi'an 710018, China
[2] Engineering Research Center of Photovoltaic Technologies and Systems, Universities of Shaanxi Province, Xi'an Jiaotong University City College, Xi'an 710018, China
* Correspondence: 18091291609@163.com

Abstract

Non-diffracting beams play crucial roles in the field of free-space optical communication due to their robust resistance to distortion in atmospheric turbulence. As a non-diffracting beam characterized by multiple parameters, the Tricomi beam exhibits great versatility and adjustability, attracting considerable interest recently. In this paper, we study the propagation properties of Tricomi beam in atmospheric turbulence based on the theory of random phase screen. It is found that the performance of Tricomi beam in atmospheric turbulence shows strong dependence on its asymmetric constants, topological charge, and half-cone angle. Meanwhile, the Tricomi beam manifests superior resistance to distortion and spatial mode stability in contrast to the conventional non-diffracting Bessel beam. Our work provides a valuable theoretical foundation for the design and performance optimization of next-generation free-space optical communication systems, potentially enabling enhanced data transmission fidelity over long atmospheric paths.

Keywords: non-diffracting Tricomi beam; atmospheric turbulence; propagation properties

1. Introduction

The advancement of efficient wireless optical communication in free space is important for enabling the next-generation high-speed data transmission [1–5] and can further promote the development of cloud computing [6], quantum information [7], and artificial intelligence [8], to name a few. The wireless optical communication has huge advantages in bandwidth [9,10] and directionality [11] in contrast to conventional radio-frequency-based systems, which means high channel capacity, enhanced data security, and robust resistance to electromagnetic interference. However, the practical performance and reliability of terrestrial and near-earth free-space optical links are predominantly constrained by atmospheric channel impairments. Among these, the atmospheric turbulence, characterized by random fluctuations in the refractive index of air due to temperature and pressure inhomogeneities [12], is widely regarded as one of the most critical and performance-determining factors [13–15]. The atmospheric turbulence directly and profoundly perturbs a propagating laser wavefront, inducing deleterious effects including beam wandering [16], scintillation [17], phase distortion [18], and so on. These phenomena degrade both the fidelity of received communication signals and the resolution of imaging systems operating in the atmospheric environment. For structured beams carrying spatial phase singularities [19], such turbulence-induced wavefront distortions may further disturb the modal

Check for updates

Received: 24 April 2026
Revised: 10 May 2026
Accepted: 14 May 2026
Published: 15 May 2026

Copyright: © 2026 by the authors. Licensee MDPI, Basel, Switzerland. This article is an open access article distributed under the terms and conditions of the Creative Commons Attribution (CC BY) license.

composition of the beam, including its orbital-angular-momentum-related characteristics. Meanwhile, when a helical phase factor $\exp(il\varphi)$ is introduced, the integer l, namely the topological charge, characterizes the phase winding and the corresponding OAM mode of the beam. This structured phase degree of freedom is important for mode manipulation and OAM-based optical communication [20,21], but it is also sensitive to turbulence-induced modal coupling.

Therefore, exploring methods to enhance the stability of light beam propagation through atmospheric turbulence is of significant practical importance. A key approach in this regard involves optimizing the beam shape. Numerous works demonstrate that the non-diffracting Bessel beams have significant advantages in reducing turbulence effects and improving link performance in free-space optical communication systems [22–24]. This robustness stems from their self-healing nature and structured wavefronts formed by conical waves. When turbulence induces local phase distortions, the undistorted peripheral waves can reconstruct the central core. In 2015, Kovalev et al. proposed a novel concept of complex-shifted non-diffracting beams [25]. Based on this work, Zhu et al. provided a generalized representation known as Tricomi beams [26]. Their complex amplitude is described by the Tricomi function and characterized by four parameters, including the half-cone angle, topological charge, and two asymmetry constants. By tuning these parameters, Tricomi beams can continuously transform among ordinary Bessel beams, off-axis Bessel beams, asymmetric Bessel beams, and sheet-like nondiffracting beams. Among them, the topological charge determines the azimuthal phase winding, while the half-cone angle and asymmetry constants control the angular-spectrum distribution and transverse morphology. It is notable that the Tricomi function can be converted to the Bessel function. Through varying the asymmetry constants, non-diffracting Tricomi beams can be converted into symmetric, asymmetric, or off-axis Bessel beams [27,28]. Compared with conventional Bessel beams, Tricomi beams exhibit richer and more complex morphologies in propagation [29–32]. Until now, the propagation properties of the Tricomi beams and their derived variants are extensively studied in many representative media, such as the gradient index medium [33], chiral medium [34], and nonlocal nonlinear medium [35]. However, the propagation properties of the Tricomi beams in atmospheric turbulence remain to be explored. Such a subject is valuable for exploiting the application potential of the Tricomi beams in wireless optical communication.

In this paper, a detailed investigation on propagation properties of the Tricomi beam in atmospheric turbulence is conducted. Based on the Von Kármán power spectral density functions, we establish the propagation model of the Tricomi beam in atmospheric turbulence by the random phase screen method. The effects of the half-cone angle, topological charge, and asymmetry constants on the performance of the Tricomi beam are numerically simulated and theoretically analyzed in terms of the helical spectrum, scintillation index, beam wander, and bit error rate. Here, the helical spectrum is used to quantify the redistribution of OAM components and thus provides a direct indicator of spatial-mode stability under turbulence. It is presented that the Tricomi beam with greater asymmetry constants exhibits superior resistance to distortion and spatial mode stability than the conventional Bessel beam. In addition, enlarging the half-cone angle and topological charge can effectively suppress the beam scintillation and wander. These outcomes will provide critical support for future wireless optical communication systems to achieve enhanced performance in long-range turbulent environments.

2. Theoretical Formula

The phase distortions induced by atmospheric turbulence can be modeled as random variables, with ensemble averages used to statistically characterize their effects on optical

beams. It means that the effect of atmospheric turbulence can be viewed as a complex phase distortion. Therefore, the propagation process of the non-diffracting Tricomi beam in atmospheric turbulence can be numerically simulated by the random phase screen method, as shown in Figure 1. As the basis, we will derive the explicit analytical expressions for the Tricomi beam. The complex amplitude of the non-diffracting beams exactly satisfies the scalar Helmholtz equation. In Cartesian coordinates (x, y, z), the general solution of the scalar Helmholtz equation can be expressed using a simplified Whittaker integral [36,37].

$$\psi(x, y, z) = \exp(ik_z z) \int_0^{2\pi} f(\varphi) \exp[ik_t(x\cos\varphi + y\sin\varphi)]\mathrm{d}\varphi, \tag{1}$$

where $f(\varphi)$ is the angular spectrum of the scalar field $\psi(x, y, z)$, $k_t = k\sin\theta_0$ and $k_z = k\cos\theta_0$ are the transverse and longitudinal components of the wave vector, with k and θ_0 being the wave number and half-cone angle, respectively. Following the work of Zhu et al. [26], the angular spectrum of the non-diffracting Tricomi beams has the form

$$f(\varphi) = \exp[ik_t(\alpha\cos\varphi + \beta\sin\varphi) - il\varphi]/2\pi, \tag{2}$$

where α and β are complex constants for describing the asymmetry of the beams, and l is the topological charge. Using the Tricomi function

$$C_s(x) = \sum_{r=0}^{\infty} \frac{(-1)^r}{r!(s+r)!} x^r, \tag{3}$$

the term $\exp[ik_t(\alpha\cos\varphi + \beta\sin\varphi)]$ can be written as

$$\exp[ik_t(\alpha\cos\varphi + \beta\sin\varphi)] = \sum_{s=-\infty}^{\infty} C_s\left(\frac{\alpha^2+\beta^2}{4}k_t^2\right)\left(\frac{i\alpha+\beta}{2}k_t\right)^s \exp(is\varphi). \tag{4}$$

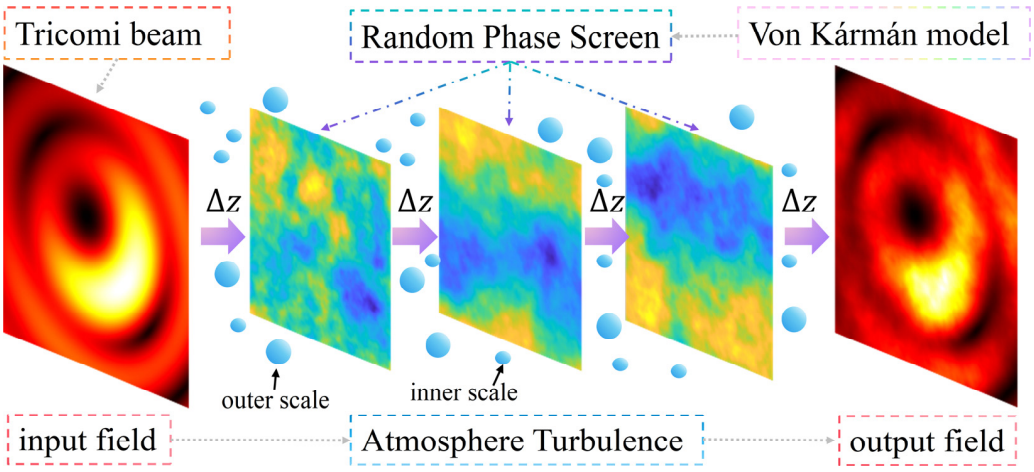


Figure 1. Schematic of the propagation of Tricomi beam in atmospheric turbulence. Turbulence is characterized by a cascade of energy through eddy hierarchies, ranging from large energy-containing scales (outer scales) to small dissipative scales (inner scales). The numerical simulation method is the random phase screen method, which initiates at z = 0 with the vortex beam's initial field, undergoing an initial vacuum propagation over a distance of Δz.

Substituting Equation (4) into Equation (2) and using the mathematical relation between the n-th order Tricomi function $C_s(x)$ and the s th-order Bessel function $J_s(x)$,

$$C_s(x) = x^{-s/2} J_s\left(2\sqrt{x}\right), \tag{5}$$

we obtain

$$f(\varphi) = \sum_{s=-\infty}^{\infty} J_s\left[k_t\sqrt{\alpha^2+\beta^2}\right]\left[\frac{\beta+i\alpha}{\sqrt{\alpha^2+\beta^2}}\right]^s \exp[i(s-l)\varphi]/2\pi. \tag{6}$$

Then substituting Equation (6) into Equation (1) and finishing the integral over φ, we can obtain the scalar field of the Tricomi beams,

$$\psi(x,y,z) = i^l \exp(ik_z z) J_l\left(k_t\sqrt{(x+\alpha)^2+(y+\beta)^2}\right)\left[\frac{i(x+\alpha)+(y+\beta)}{i(x+\alpha)-(y+\beta)}\right]^{l/2}. \tag{7}$$

It should be noted that Equation (7) describes an ideal but not physically realizable non-diffracting Tricomi beam with infinite transverse profile and energy. In practical optical systems, such an ideal field can be approximated by introducing a Gaussian aperture, leading to a Tricomi–Gauss beam $\psi_{TG}(x,y,0) = \psi(x,y,0)\exp[-(x^2+y^2)/w_0^2]$ with beam waist w_0 at the input plane. The Gaussian factor truncates the outer transverse region of the ideal Tricomi beam and makes the total energy finite, while the central asymmetric nondiffracting structure is preserved when the aperture is sufficiently large. Similar to other finite-aperture Bessel-type beams, the Tricomi–Gauss beam can maintain its quasi-nondiffracting behavior only within an effective propagation distance, which approximately scales as $w_0/\tan\theta_0$.

The specific process of the random phase screen method [38–41] is illustrated in Figure 2. The initial input field is defined as $U_0(x,y) = \psi(x,y,0)$, and U_{1-} and U_{1+} respectively denote the field before and after the phase screen. When the beam reaches the first phase screen, it has already propagated a certain distance Δz in vacuum. The vacuum beam propagation in the frequency domain can manifest as filtering via the function

$$U_f(\kappa_x,\kappa_y) = \exp\left(i\sqrt{\kappa_0^2-\kappa_x^2-\kappa_y^2}\Delta z\right), \tag{8}$$

where κ_x and κ_y denote the spatial wave numbers, and $\kappa_0 = 1/L_0$. Hence, at the first phase screen, the expression of the field is

$$U_{1-}(x,y) = F^{-1}\left\{F[U_0(x,y)]U_f(\kappa_x,\kappa_y)\right\}, \tag{9}$$

where F and F^{-1} denote the Fourier transform and inverse Fourier transform, respectively. When the beam passes through the first phase screen, its field will gain an additional phase as

$$U_{1+}(x,y) = U_{1-}(x,y)\exp[i\beta(x,y)], \tag{10}$$

in which $\beta(x,y)$ is the random phase function. Then, it is determined whether the transmission distance reaches the total link distance L. If not, the parameters are updated as $U_0 = U_{1+}$ and $z = z+\Delta z$, and such a process is repeated until the total link distance is reached.

The generation of $\beta(x,y)$ is illustrated as follows. According to Kolmogorov's theory, the phase fluctuations are described by [42]:

$$\left\langle[\phi(\mathbf{r}_1)-\phi(\mathbf{r}_2)]^2\right\rangle = 6.88|(\mathbf{r}_1-\mathbf{r}_2)/r_0|^{5/3}, \tag{11}$$

where $\phi(\mathbf{r}_1)$ and $\phi(\mathbf{r}_2)$ represent phase fluctuations at two locations $\mathbf{r}_1$ and $\mathbf{r}_2$. A key atmospheric parameter, the Fried parameter r_0, quantifies the cumulative effect of optical

aberrations encountered along a light beam's propagation path and can be derived from the refractive index structure constant C_n^2 as follows [43]:

$$r_0 = \left(0.423k^2 \int_0^L C_n^2(z)(z/L)^{5/3} \mathrm{d}z\right)^{-3/5}, \tag{12}$$

where L is the total link distance. The greater C_n^2 represents the stronger the atmospheric turbulence. For convenience, we assume C_n^2 is a constant along the propagation channel in this work. The Von Kármán turbulence model is commonly employed for simulating turbulence-induced phase screens, parameterized by the Fried parameter r_0, outer scale L_0, and inner scale l_0. In this model, the power spectrum can be expressed as [44–46]

$$\Phi_n(\kappa_x, \kappa_y) = 0.49 r_0^{-5/3} \exp\left[-\left(\kappa_x^2 + \kappa_y^2\right)/\kappa_m^2\right]\left(\kappa_x^2 + \kappa_y^2 + \kappa_0^2\right)^{-11/6}, \tag{13}$$

with $\kappa_m = 5.92/l_0$. Using the complex Gaussian stochastic matrix $H(\kappa_x, \kappa_y)$ to filter the square root of the power spectrum and then performing an inverse Fourier transform, we can obtain the random phase function as [47,48]

$$\beta(x, y) = F^{-1}\left[H(\kappa_x, \kappa_y)\sqrt{\Phi_n(\kappa_x, \kappa_y)}\right]. \tag{14}$$

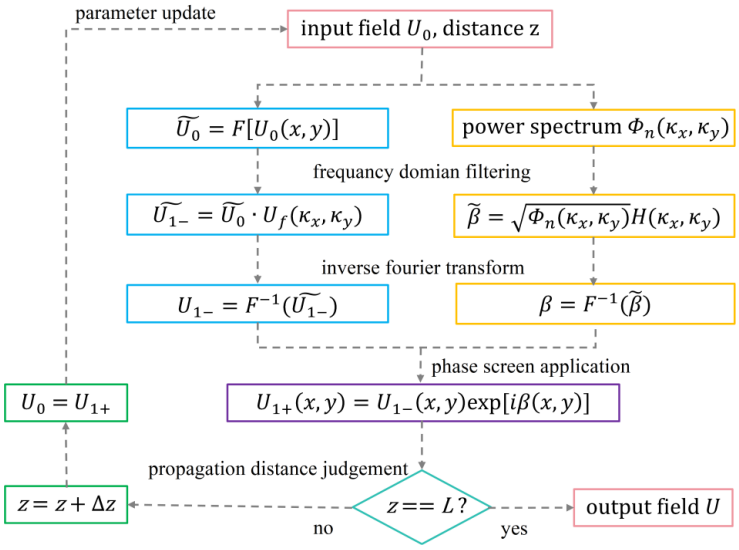


Figure 2. Schematic of the specific calculation process for the random phase screen method. Here, F and F^{-1} denote the Fourier transform and inverse Fourier transform, respectively. $U_f(\kappa_x, \kappa_y)$ and $H(\kappa_x, \kappa_y)$ are the frequency domain filtering functions for beam angular spectrum and turbulence power spectrum, respectively. L is the total link distance.

In this work, the performance of the Tricomi beam in atmospheric turbulence will be characterized by helical spectrum, scintillation index, beam wander, and bit error rate. The helical spectrum is an essential metric for assessing the quality of orbital angular momentum (OAM) states for structured light during propagation. Its physical significance lies in quantifying the purity and stability of an optical vortex beam's OAM composition at the receiver. The measurement of helical spectrum provides a direct metric for evaluating OAM-mode purity and turbulence-induced modal crosstalk that occur when such complex beams interact with media like turbulent atmosphere. Using a different spiral harmonic

factor $\exp(il\phi)$ to expand Tricomi beam, the expansion coefficient of the corresponding l modes in the beam can be obtained in (r, ϕ, z) as

$$a_l(r,z) = \int_0^{2\pi} \psi(r,\phi,z)\exp(-il\phi)d\phi/\sqrt{2\pi}, \tag{15}$$

in which, $\psi(r,\phi,z)$ is the complex field of Tricomi beam expressed in coordinates (r,ϕ,z). Thus, the energy of the l th-order spiral harmonic factor is

$$E_l = \int_0^{\infty} |a_l(r,z)|^2 r dr. \tag{16}$$

The helical spectrum is given by

$$P_l = E_l / \sum_{i=-\infty}^{\infty} E_i. \tag{17}$$

The scintillation index is another important metric for evaluating atmospheric transmission quality and is used to quantify the characteristics of random fluctuations in light intensity I at the receiver, calculated as

$$m^2 = \left\langle I^2 \right\rangle / \langle I \rangle^2 - 1, \tag{18}$$

where $\langle \cdot \rangle$ denotes the ensemble average. In practice, we will simulate this value many times and take the average.

The beam wander is manifested as the mean square error (MSE) of the in-plane light intensity centroid displacement relative to its original position during propagation, which can be expressed as

$$\sigma^2 = \frac{1}{N}\sum_{k=1}^{N}\left[\left(x_c^{(k)} - x_0\right)^2 + \left(y_c^{(k)} - y_0\right)^2\right], \tag{19}$$

where N is the number of independent turbulence realizations, k is the index of the realization, $x_c^{(k)} = \left\langle x \cdot I_c^{(k)} \right\rangle / \left\langle I_c^{(k)} \right\rangle$ and $y_c^{(k)} = \left\langle y \cdot I_c^{(k)} \right\rangle / \left\langle I_c^{(k)} \right\rangle$ denote the centroid coordinates of the received beam in the k-th realization, $x_0 = \langle x \cdot I_0 \rangle / \langle I_0 \rangle$ and $y_0 = \langle y \cdot I_0 \rangle / \langle I_0 \rangle$ denote the centroid coordinates of the initial beam, I_0 and $I_c^{(k)}$ respectively denote the light intensity at the receiver in free-space and atmospheric turbulence.

For the free-space optical links, bit error rate is evaluated as [49]

$$\mathrm{BER} = \frac{1}{2}\int_0^{\infty} p(u)\mathrm{erfc}\left(\frac{\mathrm{SNR}\cdot u}{2\sqrt{2}}\right)\mathrm{d}u, \tag{20}$$

where erfc() is a complementary error function and SNR denotes the signal to noise ratio. The probability density function is

$$p(u) = \frac{1}{u\beta_n\sqrt{2\pi}}\exp\left(-\frac{\left(\ln u + 0.5\beta_n^2\right)^2}{2\beta_n^2}\right), \tag{21}$$

where β_n^2 denotes variance of scintillation noise and will be found using Equation (18),

$$\beta_n^2 = M^2 R_p^2 m^2 \langle I \rangle^2. \tag{22}$$

Here M refers to magnification factor and R_p indicates responsivity of the photodiode. We set the magnification factor to 50 and the responsivity to 0.5 considering the

average values of commercial photodiodes. At the same SNR, a lower BER indicates better communication performance.

3. Results and Discussion

Based on the above theoretical framework and simulation method, we explore the performance of Tricomi beam in atmospheric turbulence as follows. Unless specified otherwise, the simulation parameters are as follows: inner scale $l_0 = 0.01$ m, outer scale $L_0 = 10$ m, and weak (strong) refractive index structure constant $C_n^2 = 10^{-15}$ m$^{-2/3}$ ($C_n^2 = 10^{-13}$ m$^{-2/3}$) for the atmospheric turbulence; wavelength $\lambda = 0.6$ μm, asymmetric constants $\alpha = \beta = 0.5i$, topological charge $l = 2$, and half-cone angle $\theta_0 = 0.003^\circ$ for the Tricomi beam; spacing distance $\Delta z = 5$ m and total link distance L = 300 m for the phase screen method. The size of the phase screen is 100 mm $\times$ 100 mm, and the spatial sampling and frequency interval are respectively 0.1 mm and $\pi/50$ mm. The light parameters can be flexibly tuned by space light modulators in the experiment. Notably, the selected wavelength is mainly used for proof-of-principle simulation and visualization of the propagation behavior.

First, we plot the intensity and phase of the Tricomi beams with different asymmetry constants in Figure 3. For the case of $\alpha = \beta = 0$ shown in Figure 3(a1,a2), the Tricomi beam reduces to a conventional Bessel beam, characterized by a series of perfectly concentric rings. When the asymmetry constants are introduced as $\alpha = \beta = 0.5i$, as shown in Figure 3(b1,b2), the intensity profile undergoes a significant transformation: the circular symmetry is broken, and the beam adopts a distinct crescent-shaped morphology. This deformation arises from the complex-valued asymmetry parameters, which effectively introduce a transverse phase gradient, shifting the energy distribution laterally. As the α and β increase further to $2i$, as shown in Figure 3(c1,c2), the beam structure evolves into a single sheet-like pattern, with energy concentrated predominantly along one lateral direction. Notably, for all non-zero imaginary α and β, the centroid of the Tricomi beam is displaced off-axis, in contrast to the on-axis nature of standard Bessel beams. This lateral shift is intrinsically linked to the imaginary parts of the asymmetry constants, which impart a linear phase tilt across the beam profile. These phenomena indicate that, when α and β are purely imaginary and their magnitudes grow, the resulting sheet-like intensity distribution becomes more localized, with energy increasingly confined within a narrower region. Concurrently, the spatial extent of this sheet pattern scales proportionally with $|\alpha|$ and $|\beta|$, indicating a direct controllability over the beam's transverse size through these parameters.

Figure 4 depicts the intensity and helical spectra of the Tricomi beams propagating in free-space or atmospheric turbulence for different asymmetric constants. In the case of a Bessel beam shown in Figure 4(a1–a3), the helical spectrum energy is concentrated in a single orbital angular momentum (OAM) mode. Differently, Tricomi beams with the same topological charge distribute their spectral power over multiple OAM modes, with the number of excited modes increasing for larger asymmetry parameters. It can be observed that strong atmospheric turbulence distorts the profiles of Tricomi beams and disrupts their normal OAM mode composition. However, the extent of OAM mode degradation depends noticeably on the asymmetric constants. Under strong atmospheric turbulence, the Bessel beam retains only 63% of its true OAM power and generates numerous false OAM modes. Such crosstalk is detrimental to practical OAM optical communication because it reduces the distinguishability of different OAM channels and lowers the fidelity of mode detection. In contrast, Tricomi beams preserve a substantially higher fraction of true OAM power, with the retained proportion increasing for larger asymmetry parameters. In an OAM-multiplexed communication link, a more stable helical spectrum corresponds to weaker off-diagonal terms in the mode-crosstalk matrix, which is beneficial for suppressing

interchannel interference and reducing BER [50]. This behavior occurs because Tricomi beams initially carry more OAM modes, allowing turbulence effects to disperse across each mode and thereby reduce the distortion per mode. It is noted that the improved stability observed for larger asymmetric constants should not be interpreted as an improvement of the single-OAM-mode detection probability [51].

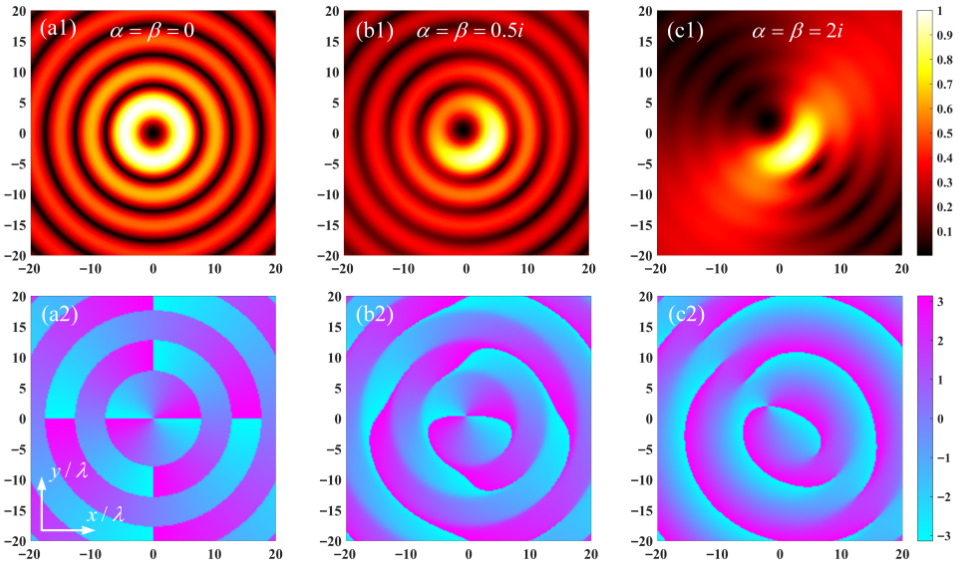


Figure 3. Normalized intensity and phase distributions of the Tricomi beams with different asymmetric constants α, β. (**a1**,**a2**) $\alpha = \beta = 0$. (**b1**,**b2**) $\alpha = \beta = 0.5i$. (**c1**,**c2**) $\alpha = \beta = 2i$.

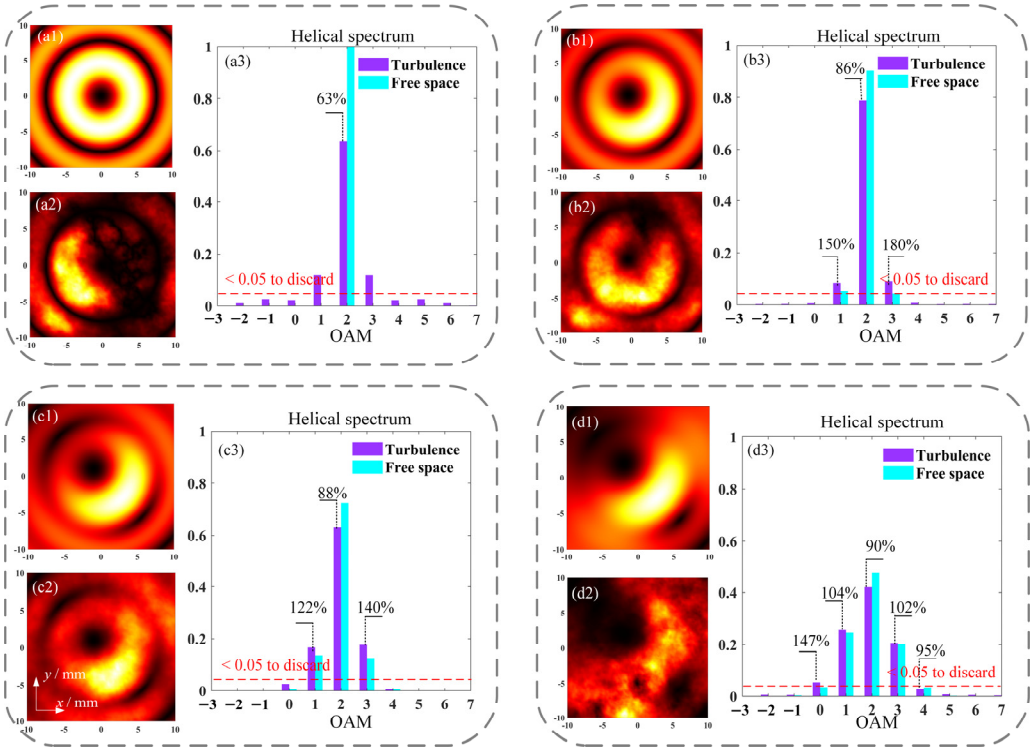


Figure 4. Intensity and helical spectra of Tricomi beams propagating in free-space or atmospheric turbulence for different asymmetric constants α, β. (**a1**–**a3**) $\alpha = \beta = 0$. (**b1**–**b3**) $\alpha = \beta = 0.5i$. (**c1**–**c3**) $\alpha = \beta = i$. (**d1**–**d3**) $\alpha = \beta = 2i$. The percentages in helical spectra represent the ratio between energies of the same OAM state in cases of free-space and atmospheric turbulence. Considering the difficulties of modulation and detection, the OAM modes with power less than 0.05 are discarded.

From Figure 5, we can explore the effects of asymmetric constants α, β, topological charge l, and half-cone angle θ_0 on scintillation index m^2 of Tricomi beams propagating in weak and strong atmospheric turbulence. The simulation results in Figure 5(a1,a2,c1,c2) show that increasing the asymmetric constants and half-cone angle can effectively suppress the beam scintillation in atmospheric turbulence. Unlike a localized obstruction, atmospheric turbulence introduces distributed random phase perturbations along the propagation path, which degrade the ideal nondiffracting character by disturbing the phase relation among conical-wave components. Therefore, the improved stability of Tricomi beams observed here should not be attributed solely to self-healing [52], but rather to the combined effects of partial conical-wave self-reconstruction, spatial averaging over transverse wave-vector components, and modal-structure stability under turbulence. Regarding the topological charge, the scintillation index is significantly reduced when l increases from 2 to 4, whereas a further increase to l = 6 produces only a slight additional improvement, as shown in Figure 5(b1,b2). This behavior can be understood from the phase topology and transverse energy distribution of the vortex field. A larger topological charge introduces a stronger azimuthal phase gradient and generally expands the characteristic annular structure of the beam. As a result, the optical field samples more independent turbulent fluctuations along the azimuthal direction, and the random phase perturbations can be partially averaged in the received intensity. This spatial-averaging effect helps suppress scintillation.

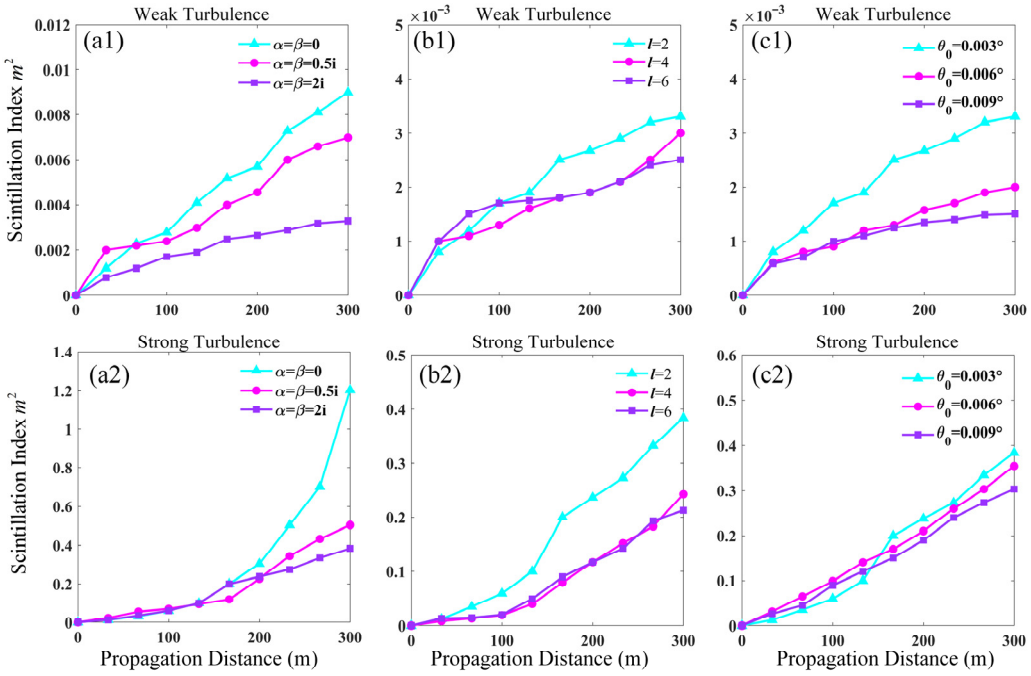


Figure 5. Scintillation index m^2 of Tricomi beams propagating in (**a1**–**c1**) weak and (**a2**–**c2**) strong atmospheric turbulence for different asymmetric constants α, β, topological charge l, and half-cone angle θ_0.

Next, the MSE of beam wander σ^2 of Tricomi beams propagating in weak and strong atmospheric turbulence for different asymmetric constants α, β, topological charge l, and half-cone angle θ_0 are demonstrated in Figure 6. As the asymmetric constants increase, as shown in Figure 6(a1,a2), the MSE of beam wander decreases correspondingly, which indicates that the more localized Tricomi beam is more beneficial to the centroid stability in beam propagation. The increased topological charges in Tricomi beams are associated with reduced beam wander under atmospheric turbulence. Higher-order vortex modes [53] are less dominated by local intensity perturbations near the beam center and exhibit stronger

azimuthal averaging of turbulence-induced distortions. Consequently, the centroid fluctuation of the received beam is reduced, as shown in Figure 6(b1,b2). In addition, enlarging the half-cone angle can also suppress the beam wander, for the reason that a larger half-cone angle corresponds to a broader angular spectrum, incorporating a greater distribution of transverse wave vector components, as shown in Figure 6(c1,c2). This diversified momentum profile allows the beam to sample a wider range of spatial frequencies, thereby averaging out the localized tip and tilt effects induced by atmospheric turbulence.

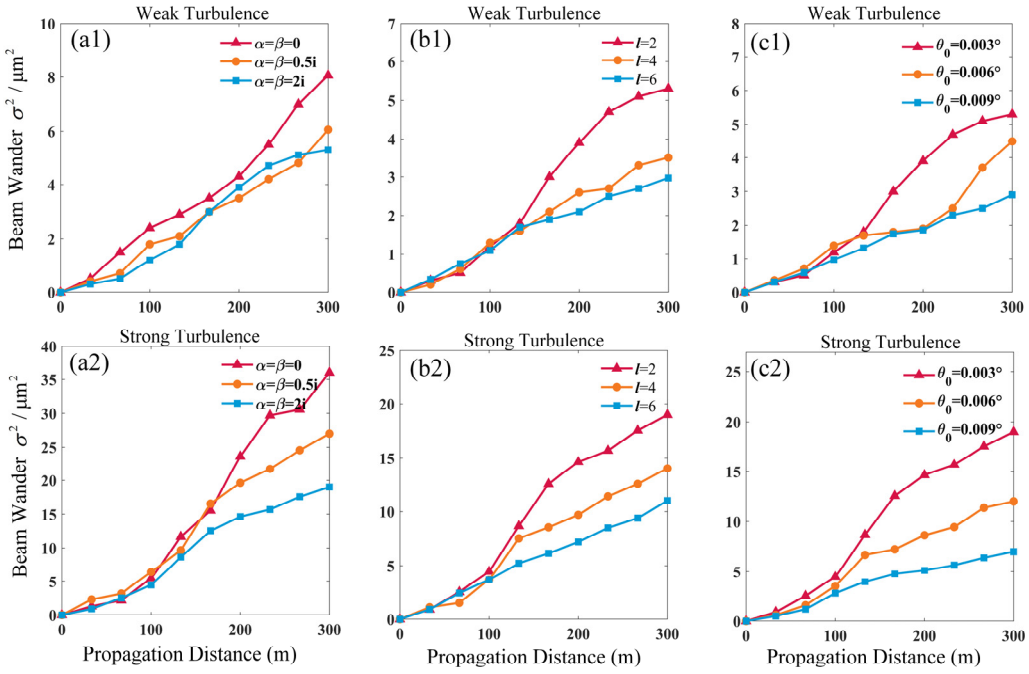


Figure 6. Mean square error (MSE) of beam wander σ^2 of Tricomi beams propagating in (**a1**–**c1**) weak and (**a2**–**c2**) strong atmospheric turbulence for different asymmetric constants α, β, topological charge l, and half-cone angle θ_0.

Finally, the communication performance of Tricomi beams under atmospheric turbulence is quantitatively evaluated through bit error rate (BER) analysis. The BER results of Tricomi beams propagating in weak and strong atmospheric turbulence are shown in Figure 7 for different asymmetric constants α, β, topological charges l, and half-cone angles θ_0. It reveals that Tricomi beams consistently exhibit superior communication stability relative to conventional Bessel beams in the presence of atmospheric turbulence, as shown in Figure 7(a1,a2). This advantage is manifested in measurably lower BER values across all simulation conditions, and the stability can be further optimized by increasing asymmetric constants. Such improvement is directly correlated with the enhanced spatial mode stability and suppressed scintillation index observed in previous analyses. Meanwhile, the Tricomi beams with higher topological charges and larger half-cone angle possess the lower BER, as shown in Figure 7(b1,b2). For the topological charge, the BER reduction exhibits a trend of diminishing returns. Specifically, beyond an optimal threshold, further increases yield negligible performance gains. Conversely, no such saturation is observed within the studied range for the half-cone angle, suggesting its role as a more linearly scalable parameter for enhancing turbulence resilience in optical communication links employing Tricomi beams, as shown in Figure 7(c1,c2).

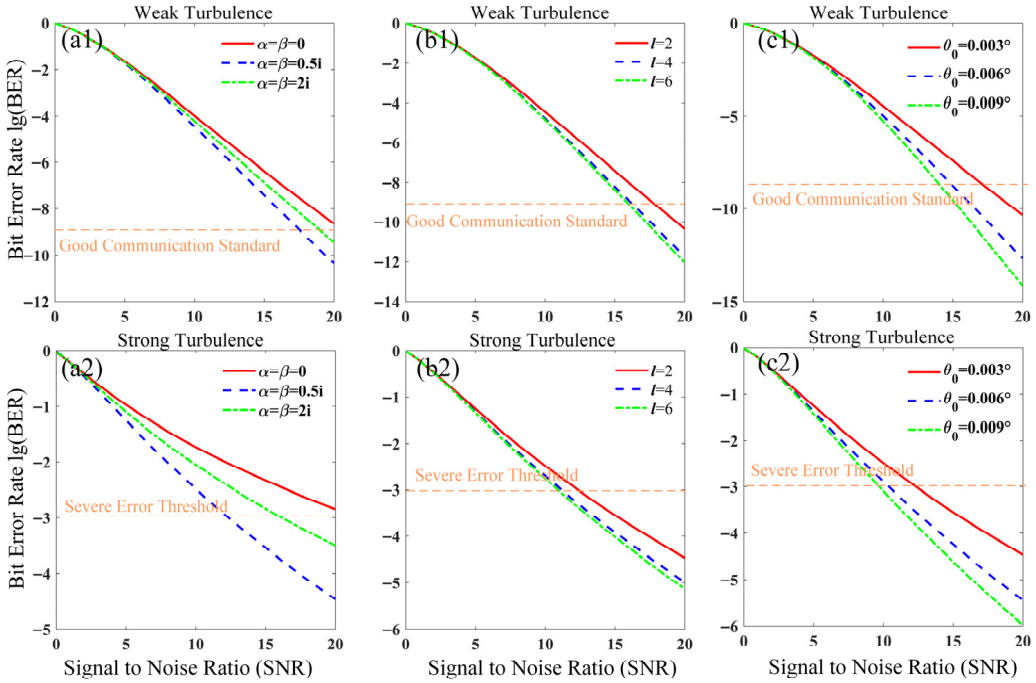


Figure 7. Bit error rate of Tricomi beams propagating in (**a1**–**c1**) weak and (**a2**–**c2**) strong atmospheric turbulence for different asymmetric constants α, β, topological charge l, and half-cone angle θ_0. For convenience, the bit error rate is presented as lg(BER). Generally speaking, the 10×10^{-3} is the severe error threshold and 10×10^{-6} is the good communication standard for BER.

4. Conclusions

In conclusion, we have reported a theoretical investigation on the propagation properties of non-diffracting Tricomi beam with a high degree of adjustability in atmospheric turbulence. Based on the random phase screen theory, a propagation model for the Tricomi beam under turbulent conditions is developed. Numerical simulations are conducted to analyze the helical spectrum, scintillation index, beam wander, and bit error rate of the Tricomi beam propagating through turbulence. The results indicate that, under certain conditions, the Tricomi beam exhibits superior resistance to distortion and higher spatial mode stability compared to a conventional Bessel beam. Furthermore, the larger asymmetric constants, higher topological charge, and increased half-cone angle contribute to improved communication stability of the Tricomi beam in turbulent environments. This study highlights the potential of Tricomi beam in stabilizing free-space optical links against atmospheric turbulence and provides guidance for selecting and optimizing Tricomi beam profiles in applications.

Author Contributions: Conceptualization, L.M.; Methodology, L.M.; Validation, H.N.; Formal analysis, H.N.; Investigation, X.H.; Data curation, Y.Z.; Writing—original draft, L.M.; Writing—review & editing, L.M.; Supervision, J.S. All authors have read and agreed to the published version of the manuscript.

Funding: This work is supported by "The Youth Innovation Team of Shaanxi Universities" project and The Scientific Research Project of the Youth Innovation Team of Shaanxi Provincial Department of Education (25JP099).

Data Availability Statement: The data that support the findings of this study are available upon reasonable request from the authors.

Conflicts of Interest: The authors declare no conflicts of interest.

References

1. Liu, T.; Yang, G.; Li, J.; Tong, C. High-speed avalanche photodiodes for optical communication. *Photonics Res.* **2025**, *13*, 1438–1451. [CrossRef]
2. Chen, L.; Shao, Y.; Di, Y. Underwater and water-air Optical wireless communication. *J. Light. Technol.* **2021**, *40*, 1442–1452. [CrossRef]
3. AI-Kinani, A.; Wang, C.; Zhou, L.; Zhang, W. Optical wireless communication channel measurements and models. *IEEE Commun. Surv. Tutor.* **2018**, *20*, 1939–1962. [CrossRef]
4. Xu, B.; Jin, C.; Park, J.; Liu, H.; Lin, X.; Cui, J.; Chen, D.; Qiu, J. Emerging near-infrared luminescent materials for next-generation broadband optical communications. *InfoMat* **2024**, *6*, e12550. [CrossRef]
5. Liu, Y.; Liao, S.; Sun, Q.; Song, S.; Wu, T.; Zhao, L. How cooperative communication distinguishes in wireless optical systems. *IEEE Wirel. Commun.* **2023**, *30*, 20–26. [CrossRef]
6. Yang, H.; Bai, W.; Yu, A.; Yao, Q.; Zhang, J.; Lin, Y. Bandwidth compression protection against collapse in fog-based wireless and optical networks. *IEEE Access* **2018**, *6*, 54760–54768. [CrossRef]
7. Riccardi, E.; Alejandro Justo Guerrero, M.; Pistore, V.; Seitner, L.; Jirauschek, C.; Li, L.; Davis, A.G.; Linfield, E.H.; Vitiello, M.S. Sculpting harmonic comb states in terahertz quantum cascade lasers by controlled engineering. *Optica* **2024**, *11*, 412–419. [CrossRef]
8. Ci, W.; Wang, P.; Xue, W.; Liu, T.; Qu, J.; Xu, X. Polarization-modulated multi-Mode optoelectronic synaptic transistor for sensing-memory-logic computing and optical wireless communication. *Adv. Func. Mater.* **2025**, *35*, 2424926. [CrossRef]
9. Deng, Y.; Huang, Z.; Zhu, H.; Fei, J.; Tang, C.; Ren, X.; Ding, L.; Zhu, L. Enhanced bandwidth of blue-green-light CsPbBr3 perovskite photodetectors toward underwater wireless optical communication. *Laser Photonics Rev.* **2025**, *19*, e01332. [CrossRef]
10. Shao, W.; Wang, Y.; Jia, S.; Xie, Z.; Gao, D.; Wang, W.; Zhang, D.; Liao, P.; Little, B.E.; Chu, S.T.; et al. Terabit FSO communication based on a soliton microcomb. *Photonics Res.* **2022**, *10*, 2802–2808. [CrossRef]
11. Shrestha, R.; Fang, Z.; Guerboukha, H.; Sen, P.; Hernandez-Cardoso, G.G.; Castro-Camus, E.; Jornet, J.M.; Mittleman, D.M. The effect of angular dispersion on THz data transmission. *Sci. Rep.* **2022**, *12*, 10971. [CrossRef] [PubMed]
12. Yuan, Y.; Capecelatro, J. Electrohydrodynamic generation of atmospheric turbulence. *Phys. Rev. Fluids* **2019**, *4*, 123701. [CrossRef]
13. Cang, L.; Zhao, H.; Zheng, G. The impact of atmospheric turbulence on terahertz communication. *IEEE Access* **2019**, *7*, 88685–88692. [CrossRef]
14. Pires, D.G.; Tsvetkov, D.; Sedeh, H.B.; Chandra, N.; Litchinitser, N.M. Stability of optical knots in atmospheric turbulence. *Nat. Commun.* **2025**, *16*, 3001. [CrossRef]
15. Vasylyev, D.; Semenov, A.A.; Vogel, W. Atmospheric quantum channels with weak and strong turbulence. *Phys. Rev. Lett.* **2016**, *117*, 090501. [CrossRef] [PubMed]
16. Bayraktar, M. Scintillation analysis of Weber beam in atmospheric turbulence. *Phys. Scr.* **2021**, *96*, 075504. [CrossRef]
17. Xu, J.; Mao, Y.; Chen, Y.; Xu, X.; Guo, Y. Machine learning assisted prediction for free-space continuous variable quantum teleportation. *IEEE Photonics J.* **2022**, *14*, 7639407. [CrossRef]
18. Wang, J.; Wang, Z.; Zhang, J.; Qiao, C.; Fan, C. Atmospheric turbulence induced phase distortions: The principal component analysis and optimized correction strategy. *Opt. Express* **2025**, *33*, 32649–32662. [CrossRef]
19. Ni, J.; Huang, C.; Zhou, L.; Gu, M.; Song, Q.; Kivshar, Y.; Qiu, C. Multidimensional phase singularities in nanophotonics. *Science* **2021**, *374*, eabj0039. [CrossRef] [PubMed]
20. Wang, J.; Yang, J.; Fazal, I.M.; Ahmed, N.; Yan, Y.; Huang, H.; Ren, Y.; Yue, Y.; Dolinar, S.; Tur, M.; et al. Terabit free-space data transmission employing orbital angular momentum multiplexing. *Nat. Photonics* **2012**, *6*, 488–496. [CrossRef]
21. Willner, A.E.; Pang, K.; Song, H.; Zou, K.; Zhou, H. Orbital angular momentum of light for communications. *Appl. Phys. Rev.* **2021**, *8*, 041312. [CrossRef]
22. Lu, Z.; Guo, Z.; Fan, M.; Guo, M.; Li, C.; Yao, Y.; Zhang, H.; Lin, W.; Liu, H.; Liu, B. Tunable bessel beam shaping for robust atmospheric optical communication. *J. Light. Technol.* **2022**, *40*, 5097–5106. [CrossRef]
23. Yuan, Y.; Lei, T.; Li, Z.; Li, Y.; Gao, S.; Xie, Z.; Yuan, X. Beam wander relieved orbital angular momentum communication in turbulent atmosphere using Bessel beams. *Sci. Rep.* **2017**, *7*, 42276. [CrossRef] [PubMed]
24. Yang, Y.; Jiao, L.; Zhu, Y.; He, F.; Zhang, J.; Liu, Q.; Li, L. Performance of underwater wireless optical communication using Bessel beams and acousto-optic modulator. *Opt. Lasers Eng.* **2025**, *184*, 108596. [CrossRef]
25. Kovalev, A.A.; Kotlyar, V.V.; Porfirev, A.P. Shifted nondiffractive Bessel beams. *Phys. Rev. A* **2015**, *91*, 053840. [CrossRef]
26. Zhu, J.; Zhu, K.C.; Ding, N.; Wang, T.F. Tricomi beams and nondiffracting sheet beams. *Results Phys.* **2021**, *28*, 104627. [CrossRef]
27. Shi, Y.; Cui, Z.; He, J.; Deng, M.; Wu, F. Light scattering of non-diffracting Tricomi beams by a homogeneous spherical particle. *J. Opt. Soc. Am. A* **2025**, *42*, 352–361. [CrossRef]
28. Mi, Z.; Zhao, Z.; Wei, R.; Wang, B.; Zhang, L.; Man, Z.; Ge, X. Rotation of a Tricomi-Gaussian beam and its focusing characteristics through a thin lens system. *J. Opt. Soc. Am. A* **2024**, *41*, 1381–1389. [CrossRef]

29. Singh, S.K.; Kinashi, K.; Tsutsumi, N.; Sakai, W. Tricomi-Gauss beam and its propagation characteristics. *Opt. Quant. Electron.* **2023**, *55*, 352. [CrossRef]
30. Singh, S.K.; Kinashi, K.; Tsutsumi, N.; Awatsuji, Y.; Jackin, B.J. Non-diffracting Vector Tricomi beams. *Opt. Commun.* **2026**, *608*, 133004. [CrossRef]
31. Mi, Z.; Zhao, Z.; Wei, R.; Wang, B.; Zhang, L.; Man, Z.; Ge, X. Propagation dynamics of a controllable auto-focusing annular Tricomi-Gaussian beam array. *Opt. Commun.* **2025**, *591*, 132104. [CrossRef]
32. Ren, S.; Han, M.; Cao, X.; Liu, L.; Cui, Z. Quadrupole interaction of Tricomi–Gaussian beams with atoms. *J. Opt. Soc. Am. B* **2025**, *42*, 160–167. [CrossRef]
33. Mi, Z.; Zhao, Z.; Li, S.; Wang, B.; Man, Z.; Zhang, L.; Ge, X. Symmetric and asymmetric Tricomi-Gaussian beams in a gradient-index medium. *Opt. Commun.* **2024**, *566*, 130705. [CrossRef]
34. Qiu, Y.; Liu, Z. Propagation of Tricomi-Gaussian beams in a chiral medium. *Results Phys.* **2024**, *58*, 107457. [CrossRef]
35. Pan, P.; Li, Z.; Wang, Z.; Dai, Z. Propagation dynamics of Tricomi-Gaussian beams in a strongly nonlocal nonlinear medium. *Opt. Commun.* **2025**, *592*, 132260. [CrossRef]
36. Turunen, J.; Friberg, A. Propagation-invariant optical fields. *Prog. Opt.* **2010**, *54*, 1–88.
37. Levy, U.; Derevyanko, S.; Silberberg, Y. Light modes of free space. *Prog. Opt.* **2016**, *54*, 237–281.
38. Droulias, S.; Loulakis, M.; Papazoglou, D.G.; Tzortzakis, S.; Chen, Z.; Efremidis, N.K. Inverted pin beams for robust long-range propagation through atmospheric turbulence. *Opt. Lett.* **2023**, *48*, 5467–5470. [CrossRef] [PubMed]
39. Droulias, S.; Loulakis, M.; Papazoglou, D.G.; Tzortzakis, S.; Chen, Z.; Efremidis, N.K. Vortex inverted pin beams: Mitigation of scintillations in strong atmospheric turbulence. *Opt. Lett.* **2024**, *49*, 4811–4814. [CrossRef] [PubMed]
40. Chen, C.; Chen, W.; Deng, Q.; Yang, L.; Deng, W.; Zeng, M.; Ma, Q.; Huang, Z. Study on propagation properties of orbital angular momentum modes in plasma sheath turbulence for power-exponent-phase Airy beams. *IEEE Antennas Wirel. Propag. Lett.* **2023**, *22*, 94–98. [CrossRef]
41. Deng, Q.; Wei, S.; Chen, W.; Yang, L.; Bo, Y.; Guo, L. Research on the propagation characteristics of power exponential vortex beams in hypersonic plasma turbulence. *IEEE Antennas Wirel. Propag. Lett.* **2024**, *23*, 1186–1190. [CrossRef]
42. Fried, D.L. Statistics of a geometric representation of wavefront distortion. *J. Opt. Soc. Am.* **1965**, *55*, 1427–1435. [CrossRef]
43. Andrews, L.C.; Beason, M. *Laser Beam Propagation in Random Media: New and Advanced Topics*; SPIE Press: Bellingham, WA, USA, 2023.
44. Kármán, T.V. Progress in the statistical theory of turbulence. *Proc. Natl. Acad. Sci. USA* **1948**, *34*, 530–539. [CrossRef]
45. Ostashe, V.E.; Brähler, B.; Mellert, V.; Goedecke, G.H. Coherence functions of plane and spherical waves in a turbulent medium with the von Karman spectrum of medium inhomogeneities. *J. Acoust. Soc. Am.* **1998**, *104*, 727–737. [CrossRef]
46. Dong, K.; Tao, B.; Cheng, M.; Al-Ahsab, H.; Yi, X.; Yan, X.; Liu, Q.; Guo, L. Characterizing propagation and vortex-splitting dynamics of Bessel-Gaussian beams in short-range atmospheric conditions. *Opt. Express* **2025**, *33*, 2878–2895. [CrossRef]
47. Yan, X.; Guo, L.; Cheng, M.; Li, J. Controlling abruptly autofocusing vortex beams to mitigate crosstalk and vortex splitting in free-space optical communication. *Opt. Express* **2018**, *26*, 12605–12619. [CrossRef] [PubMed]
48. Schmidt, J.D. *Numerical Simulation of Optical Wave Propagation with Examples in MATLAB*; SPIE Press: Bellingham, WA, USA, 2010.
49. Bayraktar, M.; Chib, S.; Belafhal, A. Numerical investigation of performance of mirrored Bessel beam in turbulence. *Opt. Quant. Electron.* **2023**, *55*, 814. [CrossRef]
50. Jin, Z.; Janoschka, D.; Deng, J.; Ge, L.; Dreher, P.; Frank, B.; Hu, G.; Ni, J.; Yang, Y.; Li, J.; et al. Phyllotaxis-inspired nanosieves with multiplexed orbital angular momentum. *eLight* **2021**, *1*, 5. [CrossRef]
51. Yu, L.; Zhang, Y.; Wang, J. Propagation of asymmetric Bessel mode in turbulent atmosphere. *IEEE Photonics J.* **2022**, *14*, 7354106. [CrossRef]
52. Anguiano-Morales, M. Self-healing properties of asymmetric Bessel beams. *Opt. Quant. Electron.* **2018**, *50*, 363. [CrossRef]
53. Ni, J.; Ji, S.; Wang, Z.; Liu, S.; Hu, Y.; Chen, Y.; Li, J.; Li, X.; Chu, J.; Wu, D.; et al. Unidirectional unpolarized luminescence emission via vortex excitation. *Nat. Photonics* **2023**, *17*, 601–606. [CrossRef]

Disclaimer/Publisher's Note: The statements, opinions and data contained in all publications are solely those of the individual author(s) and contributor(s) and not of MDPI and/or the editor(s). MDPI and/or the editor(s) disclaim responsibility for any injury to people or property resulting from any ideas, methods, instructions or products referred to in the content.